ADVANCED MATERIALS
www.advmat.de

Light Sheet-Based Laser Patterning Bioprinting Produces Long-Term Viable Full-Thickness Skin Constructs

*Levin Hafa, Louise Breideband, Lucas Ramirez Posada, Núria Torras, Elena Martinez, Ernst H.K. Stelzer, and Francesco Pampaloni**

Tissue engineering holds great promise for biomedical research and healthcare, offering alternatives to animal models and enabling tissue regeneration and organ transplantation. 3D bioprinting stands out for its design flexibility and reproducibility. Here, an integrated fluorescent light sheet bioprinting and imaging system is presented that combines high printing speed (0.66 mm^3/s) and resolution (9 µm) with light sheet-based imaging. This approach employs direct laser patterning and a static light sheet for confined voxel crosslinking in photocrosslinkable materials. The developed bioprinter enables real-time monitoring of hydrogel crosslinking using fluorescent recovery after photobleaching (FRAP) and brightfield imaging as well as in situ light sheet imaging of cells. Human fibroblasts encapsulated in a thiol-ene click chemistry-based hydrogel exhibited high viability (83% ± 4.34%) and functionality. Furthermore, full-thickness skin constructs displayed characteristics of both epidermal and dermal layers and remained viable for 41 days. The integrated approach demonstrates the capabilities of light sheet bioprinting, offering high speed, resolution, and real-time characterization. Future enhancements involving solid-state laser scanning devices such as acousto-optic deflectors and modulators will further enhance resolution and speed, opening new opportunities in light-based bioprinting and advancing tissue engineering.

1. Introduction

Tissue engineering is a rapidly developing interdisciplinary field that offers substantial potential for transformative advancements. A continuous progress in the techniques, materials, and culture methodologies is prompting high prospects for tissue engineering products. Such products hold the promise of replacing animal models for basic research and drug discovery, as well as facilitating tissue regeneration and organ transplantation. Animal models, despite being essential in research, exhibit limitations in faithfully recapitulating intricate aspects of human physiology and molecular mechanisms.[1,2] Ethical considerations and increasingly stringent regulatory frameworks accentuate the imperative for a transition away from animal models, especially when the principles of reduction and refinement encapsulated within the 3R concept do not apply.[3] Evidence of this shift is the recent enactment of the U.S. Food and Drug Administration (FDA) Modernization Act 2.0, which authorizes the use of alternatives to animal testing in the drug discovery process, thereby underscoring the significance of tissue engineering in the pharmaceutical industry (https://www.congress.gov/bill/117th-congress/senate-bill/5002[4]). Another crucial use for tissue engineering is the creation of organs for transplantation. Although human donors are the primary source of organs for transplant (allotransplantation), only 20% of individuals registered on the US National Transplant Waiting List received a transplant in 2020, despite advances in transplantation techniques.[5] Xenotransplantation, particularly from porcine sources, has been investigated as an alternative source for organ production. Nevertheless, xenotransplantation poses substantial challenges, such as the potential for infectious complications and extensive preventative and curative treatment regimens for patients, as well as ethical concerns.[6]

Among the array of biofabrication modalities, 3D bioprinting offers design flexibility, reproducibility, and high level of detail.[7] First developed for practical purposes by Thomas Boland's group in 2003, the system was defined as "computer-aided, jet-based 3D tissue-engineering of living human organs".[8] This technique was developed as a faster, more accurate alternative to classic tissue engineering technologies (for example, 3D cell culture in drops of an extracellular matrix-like Matrigel).[9] Since its inception, 3D bioprinting has diversified into distinct categories where

L. Hafa, L. Breideband, L. Ramirez Posada, E. H. Stelzer, F. Pampaloni
Institute of Cell Biology and Neurosciences (IZN)
Buchman Institute for Molecular Life Sciences (BMLS)
Goethe-Universität Frankfurt am Main
Max-von-Laue-Straße 15, 60438 Frankfurt am Main, Germany
E-mail: fpampalo@bio.uni-frankfurt.de

N. Torras, E. Martinez
Institute for Bioengineering of Catalonia (IBEC)
The Barcelona Institute of Science and Technology (BIST)
Barcelona 08028, Spain

The ORCID identification number(s) for the author(s) of this article can be found under https://doi.org/10.1002/adma.202306258

DOI: 10.1002/adma.202306258

3D architectural arrangement is attained through diverse modalities. According to the American Society for Testing and Materials (ASTM) standards,[10] the branch of bioprinting that achieves material deposition using physical pressure through a nozzle is divided into extrusion-based[11] and jetting-based bioprinting.[12] The former involves the constant extrusion of material, while the latter deposits biomaterial in droplet form. The speed (60 $mm^{-1}s$ for extrusion[13]) and resolution of nozzle-based bioprinting depend on the velocity and diameter of the nozzle, respectively. Those methods are limited by the shear pressure imposed by the nozzle, limiting permissible ranges of cell density and material viscosity.[13] Another branch of bioprinting leverages light-induced processes (termed Vat photopolymerization).[14] Within this context, digital light projection (DLP) benefits from the light-based crosslinking of complete planes, using an axial translation to produce 3D objects. These planes can also be generated by radon transform to provide reverse-computerized tomography (CT) stacks which are projected into a volume of photocrosslinkable polymer, the principle on which volumetric bioprinting is based.[15] This method enables fast bioprinting (in the order of a mm^3/s)[16,17] with good resolution (30 to 50 µm)[17,18] and is not limited by the viscosity of the polymer.[13] Noteworthy within these light-based volumetric techniques is xolography. In xolography, a projector illuminates a 2D pattern into a resin-filled cuvette and two counterpropagating orthogonal static light sheets activate the photoinitiator in the plane being crosslinked. By superimposing the light sheets with the projections, the resolution in the z-plane can be increased.[19] The highest resolution can be achieved with a two-photon light source as a trigger for the photocrosslinking, reaching a resolution of 0.1 µm.[20] Higher speeds of maximum 20 $mm^{-1}s$ can be achieved with this method, although the resolution in this case is ≈250 µm.[21]

While the field of bioprinting has been focusing on speed and resolution, the assessment of cell viability and function within the bioprinted tissue are done "offline" in a separate device. Consequently, bioprinting and imaging proceed as parallel, discrete processes across most platforms. Exceptions exist, some that combine live brightfield monitoring of the process.[17,22,23] Nonetheless, they do not allow for online monitoring of both the hydrogel or the cells and, so far, no mention of an integrated fluorescent imaging device has been made.

Here we present LUMINATE (Light sheet-based Ultrafast Microscopic Non-contact And Three-dimensional Enhanced bioprinting), a method that encompasses high printing speed (0.66 mm^3/s) and high resolution (9 µm) while introducing a fully integrated and streamlined fluorescent light sheet microscope capable of capturing real 3D images by optical sectioning the bioprinted construct. Using the principle of direct laser patterning, a gaussian light beam is patterned at high velocity onto a vat of photocrosslinkable material. A static light sheet is conjointly projected at a 90° angle relative to the patterned light beam, defining a spatially confined volume in which the total light dose surpasses the threshold necessary to trigger the crosslinking process, thus allowing for a confined voxel to be crosslinked. The patterned light beam, in theory, allows for a 5.7 µm x- and y-resolution (beam waist at focal point, calculations shown in Figure S13, Supporting Information) and a 49 µm z-resolution (waist of the light sheet, Figure S2, Supporting Information). With our setup 9 µm-sized features have been printed.

Table 1 compares key properties of the light sheet bioprinter with recent 3D (bio-) printers. An extensive comparison of all important properties in a 3D (bio-) printer can be found in Table S8 (Supporting Information).

Furthermore, LUMINATE incorporates a light sheet-based imaging system.[24,25] This allows to monitor the progression of hydrogel crosslinking through fluorescent recovery after photobleaching (FRAP) and to straightforwardly visualize with light sheet fluorescence microscopy (LSFM) fluorescently labeled cells in situ immediately before and immediately after the 3D bioprinting procedure. In a practical application, human fibroblasts were encapsulated in a hydrogel based on thiol-ene click chemistry by bioprinting a hollow cylinder with visible light (≈8 mm^3 printed within seconds). The process was fast and high-resolution and produced a cell-laden construct that exhibited high short- and long-term cell viability. Notably, the functional integrity of the cells was preserved, as evidenced by the expression of distinct dermal markers. Full-thickness skin constructs (encapsulated fibroblasts and subsequent co-culture with human keratinocytes in air-liquid conditions) were still viable at 41 days post-bioprinting and displayed epidermal and dermal characteristics, with evidence of basal membrane formation. Taken together, this work shows that LUMINATE is capable of high speed and definition, with the potential to achieve an even better performance.

Additionally, the successful imaging of cells and hydrogels in a streamlined fashion using the bioprinting device opens new opportunities for biologists and tissue engineers. This work aims to pave the way for further improvements: by integrating solid-state laser scanning devices operating in the MHz range, such as acousto-optic modulators (AOM), deflectors (AOD) and diffractive optical elements (DOE) in the LUMINATE system, both printing resolution and speed can be even further improved.

2. Results and Discussion

2.1. Combining Light Sheet-Based Bioprinting and Light Sheet Microscopy in One Device and One Process

LSFM was further developed in the early 2000s as a selective/single plane illumination microscope (SPIM),[24,25] using a cylindrical lens to create a coherent static light sheet illumination for the fluorescence excitation in the specimen. In SPIM, 3D image stacks are recorded by translating the specimen along the z-axis (perpendicular to the xy-plane defined by the light sheet). Multiple views of the same specimen can be recorded by rotating the specimen along the axis perpendicular to the xz-plane (θ-axis, rotation axis). Later, light sheet systems adopted a galvanometer mirror to scan an incoherent light sheet across the xy-plane, resulting in the so-called digital scanned light sheet microscopes (DSLM).[26,27] In the system presented in this study, dubbed LUMINATE, we built upon the principles of SPIM and DSLM to realize a novel light sheet-based bioprinter with light sheet fluorescence imaging capability. This allows the 3D imaging of the bioprinted specimen before, during or immediately after printing, offering novel opportunities to monitor the cell behavior and physiology in the bioprinted constructs. In LUMINATE, a static light sheet (λ = 405 nm) is generated by using a cylindrical lens. The static light sheet selectively exposes single xy-planes of the photocrosslinkable hydrogel to a light dose below

Table 1. Comparison of 3D (Bio-)printers.

3D (Bio)printer	Technique	Speed [mm^3/s]	Print time increase with volume	Resolution [µm]	Energy Dose [mJ/cm^2]	Cell viability [%]	Reference
LUMINATE	orthogonal laser-patterning	0.66	Linear	9.01	5 – 10	>90	This work
Extrusion	Fused deposition modelling	10 – 20	Linear	>100	-	>70	Gómez-Blanco et al. 2021
Stereolithographic (SLA)	LCD photomask	0.21	Linear in height	100 – 200	50	>95	Breideband et al. 2022
Stereolithographic (SLA)	Digital Light processing (DLP)	0.018	Linear in height	25	10 – 100	>85	Torras et al. 2022
Two Photon	Two Photon-Photopolymerization	0.000045 – 0.125	Linear	0.8 – 10	NA	>70	Dobos et al. 2020
Volumetric Bioprinting	Tomographic additive manufacturing	6 – 182	Same time up to 3.9 cm^3 (14 × 14 × 20 mm)	40 – 100	100 – 500	>90	Loterie et al. 2020, Bernal et al. 2022, Gehlen et al. 2023
Volumetric Bioprinting	Xolography	55	Same time up to 1 cm^3	20	50 – 300	Currently not suitable for bioprinting	Regehly et al. 2020

the crosslinking threshold. Simultaneously, a pair of galvanometer mirrors scans a laser beam across the xy-plane. The crosslinking threshold is selectively reached at the intersection of the scanned beam with the light sheet. This scheme, combined with a translation of the specimen holder along the z-axis, allows the generation of 3D illumination patterns. The patterned light (λ = 395 nm) is directed through a scan, a tube, and an objective lens. The beam is then introduced into a water-filled chamber where a custom specimen holder (or cuvette) containing a light-sensitive photocrosslinkable hydrogel (either with or without cells), is suspended (see **Figure** 1a and Figure S1, Supporting Information). This hydrogel, under the right conditions (wavelength, laser intensity and exposure time surpassing the crosslinking threshold of the hydrogel), crosslinks, resulting in a bioprinted object either free-floating in the non-crosslinked material or attached to a support (e.g., a glass slide, see **Figure** 2i-ii). In addition to bioprinting, the galvanometric mirrors are used to generate a DSLM-like light sheet at other wavelengths suitable for light sheet fluorescence microscopy. This configuration enables the capture of 3D image stacks through the technique of optical sectioning, not only for bioprinted constructs but also for a variety of large biological specimens. For imaging purposes, two complementary metal-oxice-semiconductor (CMOS) cameras are integrated in the system.

One inspection camera, positioned along in the optical axis of the patterning laser beam. (z-axis), allows to inspect both the cuvette position and the xy-pattern of the laser during printing. For light sheet fluorescence imaging, a second camera is positioned orthogonally to the z-axis according to the classical LSFM configuration. A filter wheel, equipped with an emission filters set, is placed in front of the camera to collect the fluorescence signal from the specimen. All elements of the device are shown in Figure 1b. Further details on the theoretical modeling of light sheet bioprinting are given in Figure S13 (Supporting Information).

The bioprinting setup of the LUMINATE system uses a G-code interpreter to produce a 3D laser patterning. G-code is a widely used programming language for computer numerical control (CNC) machines.[28] G-code instructions contain action commands, interpreted by the device (motion on and motion stop, positioning, turning on and off the. laser, laser intensity) and a series of xyz coordinates. During bioprinting, the system interprets the G-code commands as an angular motion of the galvanometric scanners executed at a defined speed and laser intensity. The 4f optical system translates the angular scanning of the laser beam determined by the galvanometric mirrors to an xy planar pattern. The xy pattern combined with the translation of the cuvette along the z-axis, results into a layered 3D illumination (see Figure 1c iii). LUMINATE is operated using a custom firmware written in C++ alongside a controller software written in C# steering every electronical component through a microcontroller. G-code files are uploaded to the microcontroller through the controller software and subsequently interpreted by the firmware.

During printing, the G-code file is read line-by-line. The xyz coordinates are extracted. When. a print command ("G-command") is found, the laser is turned on with at the power set in the command line, and the galvanometric scanners move the beam from the current position to a. new position defined by xy-axes coordinates. After completion of each layer's xy scanning, a. further motion command including a z-coordinate prompts the stage to move to the next layer. This process is repeated for the whole length of the G-code file. Finally, a stop command. ("M00") terminates the printing process.

Printing with the xy laser beam alone produced high-resolution structure across the xy-plane. Increasing the power of the laser beam enabled deeper penetration into the cuvette, thus reducing the number of necessary layers, and allowing faster printing times (see Figure 1c i).

A real-time demonstration of this technique can be observed in Movie S1 (Supporting Information), which showcases the single-beam xy patterning of a resolution wheel (similar to the one pictured in Figure 2a i). Nevertheless, increasing the laser power can lead to the overexposure of the initial layers of the

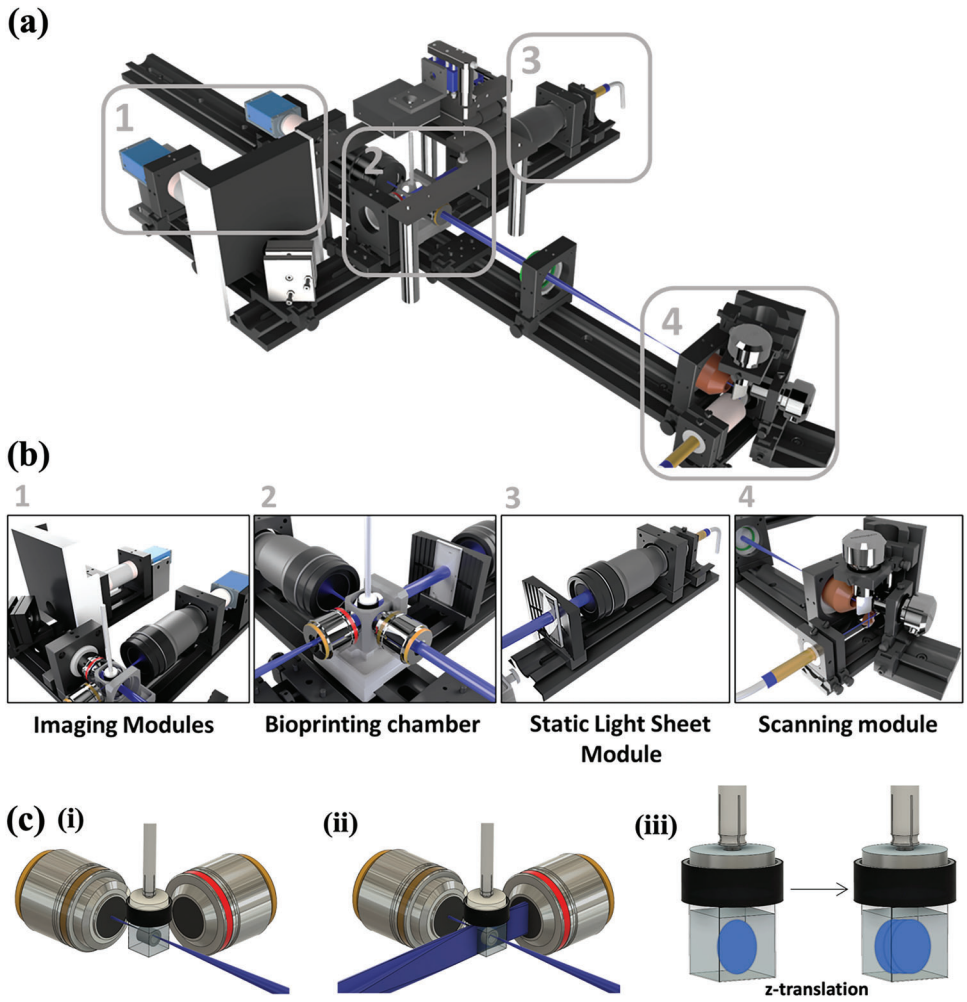

Figure 1. Overview of the light sheet bioprinter setup. a) Overview of the light sheet patterning bioprinter optical set up. b) The bioprinter consists of four distinctive modules. The imaging module (1) is capable of capturing patterns during the bioprinting process as well as fluorescence images in situ before and after bioprinting. (2) The bioprinting chamber keep deionized water steady at 37 °C to guarantee optimal conditions for cell culture and bioprinting. (3) The static light sheet is generated by a laser coupled with a beam expander and a cylindrical lens. (4) The scanning module consists of three mirrors, one 45° mirror to inject the laser beam into a galvanometric mirror pair, each one dedicated to scan the beam in a single axis (x and y). c) At the crossing of the (scanned) laser beam and the static light sheet, a cuvette made of FEP-foil contains the bioink (hydrogel and cells) for the photocrosslinking process and imaging. (i) A single laser beam or (ii) double illumination crosslinking is possible for different printing requirements. (iii) Rendering of the layer-by-layer crosslinking process using xy-patterning followed by z-translation.

printed object, inducing an enlargement of objects across the xy- plane. Moreover, complex internal structures obstructing the trajectory of the light beam would not be reproduced accurately. To achieve enhanced z-resolution, a static light sheet (λ = 405 nm) generated by a single cylindrical lens to orthogonally illuminate the bioink-laden cuvette (see Figure 1c ii). By integrating a second light source, the bioink's photocrosslinking threshold was surpassed selectively within the overlapping region of the two illumination sources—namely, the static light sheet and the laser beam. Hence, the bioprinted volume was confined to a distinct voxel, whose size is determined by the diameter of the laser beam waist along x and y and by the thickness of the static light sheet along z. The usage of the static light sheet was not affecting print speed, since the modulation of the laser engine is in the MHz range, compared to kHz range for the scan mirrors. Figure S1, Figure S2, and Movie S2 (Supporting Information) show the static light sheet in the bioprinter setup.

Customizable specimen holders or cuvettes with dimensions from 1.5 × 1.5 × 2 mm^3 to 10 × 10 × 12 mm^3 (width x length x height), made of fluorinated ethylene propylene-foil (FEP-foil) were produced based on previous work from Hötte et al.[29] FEP foil cuvettes consist of a vessel that is optically ideal for bioprinting as well as for microscopy. Indeed, the refractive index of FEP foil closely approximates that of water, minimizing optical aberration due to refractive index mismatch (FEP n = 1.34; water n = 1.33, Figure S3, Supporting Information). Moreover, the cuvettes have the advantage that 3D bioprinted constructs can be washed and cultured in the same cuvette used for bioprinting, thus allowing a streamlined process without unnecessary handling of the specimen. To achieve a cell-friendly environmental control in the bioprinter, a water-filled chamber comprising a heating

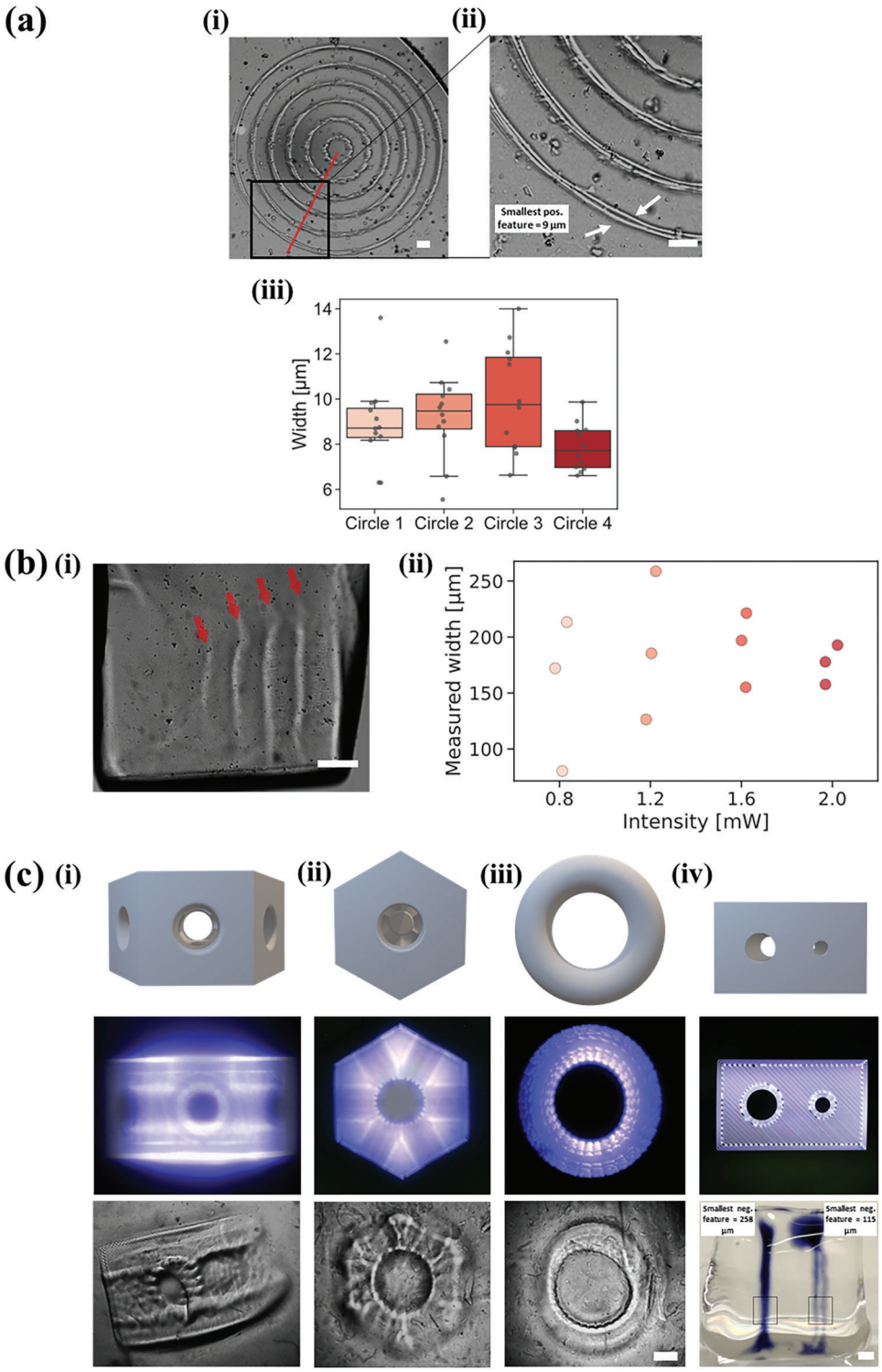

Figure 2. 3D bioprinting of complex objects is accurate when using LUMINATE. a) (i) The theoretical minimal axial crosslinking resolution of 5.7 µm (beam waist diameter) for the laser beam is nearly achieved with 9.01 µm (mean) by using Cellendes hydrogel 1 for photocrosslinking. Red line indicates where the widths of crosslinked lines were measured. Scale bar: 100 µm. (ii) Zoomed image, showing two separate crosslinked lines per circle, indicated by two white arrows. Scale bar: 100 µm. (iii) Four concentric circles were bioprinted with the lowest laser settings leading to photocrosslinking. Line widths for 12 lines per circle construct were measured and are shown here in boxplots, see Table S9 (Supporting Information) for all values. b) (i) The static light sheet produces structures that are (ii) ranging from ≈80 to 158 µm in thickness, depending on the laser power, using Cellendes hydrogel 1. Red arrows show the individual crosslinked sheets. Scale bar: 500 µm. (c) Complex objects printed with LUMINATE show high resolution. Scale bar in light pattern and brightfield pictures (applies for pictures i-iii): 1 mm. (i) Side view of a liver lobule object. Side holes are 1.2 mm in diameter. (ii)

foil and a temperature sensor was realized. The FEP-foil cuvette containing the bioink is immersed in the water-filled chamber. The chamber is equipped with a heating foil, a temperature sensor and a proportional-integral-derivative (PID) temperature controller, which ensures incubation of the cells at 37 °C. The detailed description of the specimen holder and the surrounding bioprinting chamber is shown in Figure S1 (Supporting Information).

We established a workflow for the design, patterning, and fabrication of 3D bioprinted constructs (Figure S4, Supporting Information). First, a 3D construct is modelled either by designing it in computer-aided design (CAD) software or by downloading a suitable file from internet repositories. (e.g., thingiverse.com). The exported ".stl" file is sliced into lines and layers by an open-source slicing software, resulting in a G-code file. Next, a custom Python script is used to append to the code bioprinting-specific G-code commands such as scanning speed and laser power. Using this script, additional adjustments are possible, such as the modulation of the light intensity across the z-stack. The edited G-code file is then uploaded to the bioprinter controlling software. After starting the printing, the rear camera was used to inspect the accuracy of the 3D pattern at each single illuminated planes of the structure. After patterning within the hydrogel, the rear camera is used to record high-resolution images and videos of the printed object. Next, the constructs can either be extracted from the cuvette for further culture in a multiwell-plate or left in the cuvette in situ imaging with the LSFM function of the bioprinter as described in the following.

2.2. The Light Sheet Bioprinter Produces Complex and High-Resolution Structures

While the properties of the light sheet have been extensively studied, its photocrosslinking characteristics remain yet to be fully determined. To test the performance of the LUMINATE bioprinter, hydrogel objects of varying widths and depths were 3D printed. The process of laser patterning was conducted with two distinct light-sensitive cross-linkable hydrogels. First, a thiolene photocrosslinkable hydrogel consisting of a dextran-based backbone and a hyaluronic acid crosslinker (referred to as Cellendes hydrogel 1, see Table S5, Supporting Information) was tested. Next, an acrylate-based hydrogel, a composite blend of gelatin methacrylate and poly(ethylene) glycol diacrylate (referred to as GelMA/PEGDA, see Table S6, Supporting Information) was used. The versatility of the LUMINATE bioprinting device extends to the choice of hydrogels and photoinitiators. Importantly, LUMINATE is compatible with all photo-crosslinkable hydrogels and photoinitiators, since it relies on the same photochemical reactions used by all 405 nm light-based printers. Thus, beyond the hydrogels employed in our study, a wide range of alternative hydrogel materials can be used with the device, each offering unique properties suited to specific applications in tissue engineering. Moreover, the potential for incorporating different photoinitiators opens the door to a broader spectrum of crosslinking capabilities. Notably, the LUMINATE device encompasses four laser wavelengths (395, 488, 561, and 640 nm), allowing for flexibility in activating a variety of photoinitiators.

The bioprinter's xy resolution was assessed by using a soft hydrogel suitable for cell attachment and growth (Cellendes hydrogel 1, Table S7, Supporting Information). For this test, concentric circles were printed on the surface of coverglasses. This allowed to obtain high-contrast bright-field images suitable for the reliable measurement of the smallest achievable detail with LUMINATE. In fact, images of high-resolution features floating in the surrounding liquid medium have very low contrast due to the refractive index homogeneity between polymerized and unpolymerized hydrogel (close to the one of water n = 1.33). In contrast, the index mismatch introduced by the glass substrate (n = 1.52) allows for an optimal contrast. Moreover, anchoring the crosslinked hydrogel to a surface resulted in very stable images, which also improved the reliability of the measurement (Figure 2a i,ii). In the future, the use of fluorescently labeled bioink formulation should allow us to image high-resolution details with the integrated light sheet fluorescence microscope, avoiding the use of an additional 2D substrate. Scanning the light beam twice for each concentric circle, two lines next to each other were printed. The width of the printed lines was measured to determine the xy resolution (Figure 2a iii and Figure S6, Supporting Information). The theoretical minimal axial resolution of 5.7 µm (beam. diameter at focal point, calculations shown in Figure S13, Supporting Information) was nearly achieved with 9.01 µm ±. 1.95 µm (standard deviation) on average (median: 8.72 µm). Next, the resolution achievable by the light sheet along the z-axis was tested with Cellendes hydrogel 1. Light sheets atincreasing laser power intensity (0.8, 1.2, 1.6, 2 mW) were used to crosslink single planes in. the hydrogel (Figure 2b i,ii,d Figure S7, Supporting Information). The average thickness of the light sheet-crosslinked plane at 0.8 mW was measured to be 178.2 µm ± 46.2 µm (standard deviation) and the thinnest light sheet-crosslinked plane with 0.8 mW was 80.4 µm.

It was noticed that the thickness of the photocrosslinked planes decreased linearly with decreasing intensity. These results are in accordance with the Beer-Lambert law, where the intensity of the light decreases linearly in the z-depth[31] and seems to compensate for the absorption.

Figure 2c illustrates the bioprinter's capabilities through various visualization methods: first, the designed CAD model, then the maximum intensity projection of the light pathway, and finally the resulting object. A complex model, a liver lobule (Figure 2c i,ii), was intentionally designed to encompass numerous hollow tunnels spanning the x-, y-, and z-axes. Visual assessment of the CAD rendition (depicted in the first row) alongside the illumination pattern (second row) reveals the

Top view of the liver lobule. The edges are well defined. The diameter of the central hole is 2 mm. (iii) Print of a torus. The diameter and thickness are accurate. Additionally, the shape is overall smooth, which is difficult to achieve with extrusion bioprinters. The liver lobule and torus were printed with the GELMA/PEGDA hydrogel. (iv) Microfluidic construct with designed width x height x depth of 5×3×4 mm and channel diameters of 1 and 0.5 mm were printed with Cellendes hydrogel 2 to be ready for use with cells. Construct was turned 90° with channels facing up and trypan blue was pipetted on top of channels to showcase the negative features. Smallest measured channel width for left channel was 258 µm and for right channel 115 µm. Scale bar: 500 µm.

incorporation of these intricate structures. The brightfield image captured with transmitted light (third row) effectively verifies the successful crosslinking of the resulting object, confirming its structural integrity. Next, a flat torus was designed and photocrosslinked (Figure 2c iii). A torus is characterized by positive, negative, and zero Gaussian curvatures, geometric figures that translate into varied cell morphologies and can be crucial to proper biological functions.[30] Those curvatures are known to be challenging to replicate using other types of bioprinters. LUMINATE could execute this complex task, smoothly fabricating the torus structure. Upon completion of the imaging process within LUMINATE in the unpolymerized hydrogel, the bioprinted objects were extracted from the cuvette and imaged in ambient air conditions under a stereomicroscope (see Figure S5, Supporting Information). Next, a microfluidic construct with two channels of 1 and 0.5 mm diameters was designed and 3D bioprinted (Figure 2c iv). Channels were intentionally designed with larger diameters to counteract on the swelling of the hydrogel. After printing, the construct was washed and turned 90 degrees with the channel openings facing upward. Then, trypan blue was pipetted on top to showcase the feature sizes. The smallest successfully printed negative feature was measured to be 258 µm for the left (1 mm diameter) channel. The right channel (0.5 mm diameter) turned out to be, even after washing, partially clogged resulting in an actually smaller negative feature size of 115 µm.

2.3. Quality Control of the Bioink Performed throughout the Bioprinting Process

In the previous sections, we characterized the bioprinting capabilities of LUMINATE, showing that using light sheet illumination allows a fast and efficient layer-by-layer bioprinting of 3D structures. In this section we show how leveraging the light sheet imaging capabilities inherent in the setup, a live monitoring of both hydrogel and cells immediately before and immediately after the bioprinting procedure is straightforward. This, along the real-time monitoring of the patterning beam and of the construct with bright-field microscopy, allows to comprehensively characterize the behavior of the cells and of the hydrogel throughout the whole photo-crosslinking process up to the final product.

An angiogenesis model was used, in which fibroblasts stained with a mitochondrial dye (Hs27-MitoTracker) were co-cultured with human umbilical vein endothelial cells (HUVEC) expressing green fluorescent protein (GFP-HUVEC) as spheroids – defined as cell aggregates[32]– for 48 h at a 2:1 ratio. The spheroids were then collected and resuspended in the polymer solution (Cellendes hydrogel 2, Table S7, Supporting Information) before bioprinting. The hydrogel contained low-melting agarose in low concentration that allowed the spheroids to remain in suspension. The chosen bioprinted object was a hollow cylinder (2.5 mm height, 2.5 mm diameter with 1.5 mm diameter hole, see **Figure** 3a iii and Figure S8, Supporting Information). The process took place in a 3×3×3.5 mm^3 cuvette using a single light beam an intensity of 4.81 mW. The choice of a hollow cylinder ensured efficient diffusion of medium for optimal cell growth. The cells' imaging was conducted in situ as a z-stack through the light sheet microscope, both prior to and immediately following the bioprinting procedure (Figure 3a i and Movie S3, Supporting Information).

The images show that endothelial cells positioned themselves along the periphery of the spheroid, while the fibroblasts aggregated densely at the core of the spheroids. Remarkably, no difference was discernable between the pre- and post-bioprinting images – the same parameters for the light sheet (intensity, exposure time) were used, yet the fluorophores were not affected by the intensity of the beam during printing (no visible photobleaching). Movie S3 (Supporting Information) provides a visual walkthrough along the depth of the z-stack, observed from the perspective of the GFP channel. This video showcases the spatial arrangement and distribution of GFP-HUVEC cells within the bioprinted construct. Additionally, the localization of the spheroids did not vary, indicating negligible hydrogel contraction or expansion throughout the bioprinting procedure. Furthermore, the rear camera was used to capture the precise positioning of the light patterns onto the hydrogel during the bioprinting process (not shown), along with the final product post-bioprinting (Figure 3a ii). The sharp definition of the cylinder design was distinctly discernible from both frontal and, when rotating the object, lateral perspectives. This indicated that the spheroids, albeit being dense and highly scattering cellular spheres, did not significantly affect the resolution of this object. The same picture was used to assess the placement of the spheroids in relation to the printed object. Indeed, the spatial positioning of the cells within the construct's design is crucial, especially to mimic stem cell niches or a complex tumor microenvironment. Another valuable monitoring indicator was the number of encapsulated spheroids within the final product, helping determine the efficiency of the bioprinting process in terms of cell density. Notably, the utilization of light sheet microscopy enabled the acquisition of 3D image stacks deep in the live specimen.

The assessment of the bioprinted materials' quality would not be complete without investigating the role of the hydrogel in shaping the final object. A quantitative measure of the degree of crosslinking in the hydrogel, which depends on the light intensity and the exposure time, was achieved through fluorescence recovery after photobleaching (FRAP). In previous studies, FRAP has been employed to investigate the microstructure of hydrogels by analyzing the diffusion of fluorescent dyes.[33-35] Conventional confocal microscopy has been the gold standard to image FRAP results. However, light sheet microscopy, by exciting fluorescence over a large field of view can measure lateral diffusion over a wide area of the specimen, which is invaluable to study hydrogels with a stiffness gradient. As a proof of concept, a hydrogel (Cellendes hydrogel 1) containing fluorescein isothiocyanate (FITC) coupled dextran (FITC-dextran, 20 kDa), a fluorescent dye, was crosslinked using LUMINATE. A large cube filling the whole volume of the cuvette was crosslinked (see Figure 3a iii), before analyzing the diffusion of the dye using FRAP.

Figure 3b i illustrates the three phases of FRAP. First, a baseline was recorded using a scanning light sheet, measuring the fluorescence level prior to bleaching. Next, a high intensity single beam was directed through the hydrogel to bleach the dye within the center of the image. Finally, the recovery phase ensued, wherein the return of fluorescent molecules to the bleached area was imaged and fluorescence levels were measured at regular intervals until reaching a plateau (Figure 3b i,ii). The time required

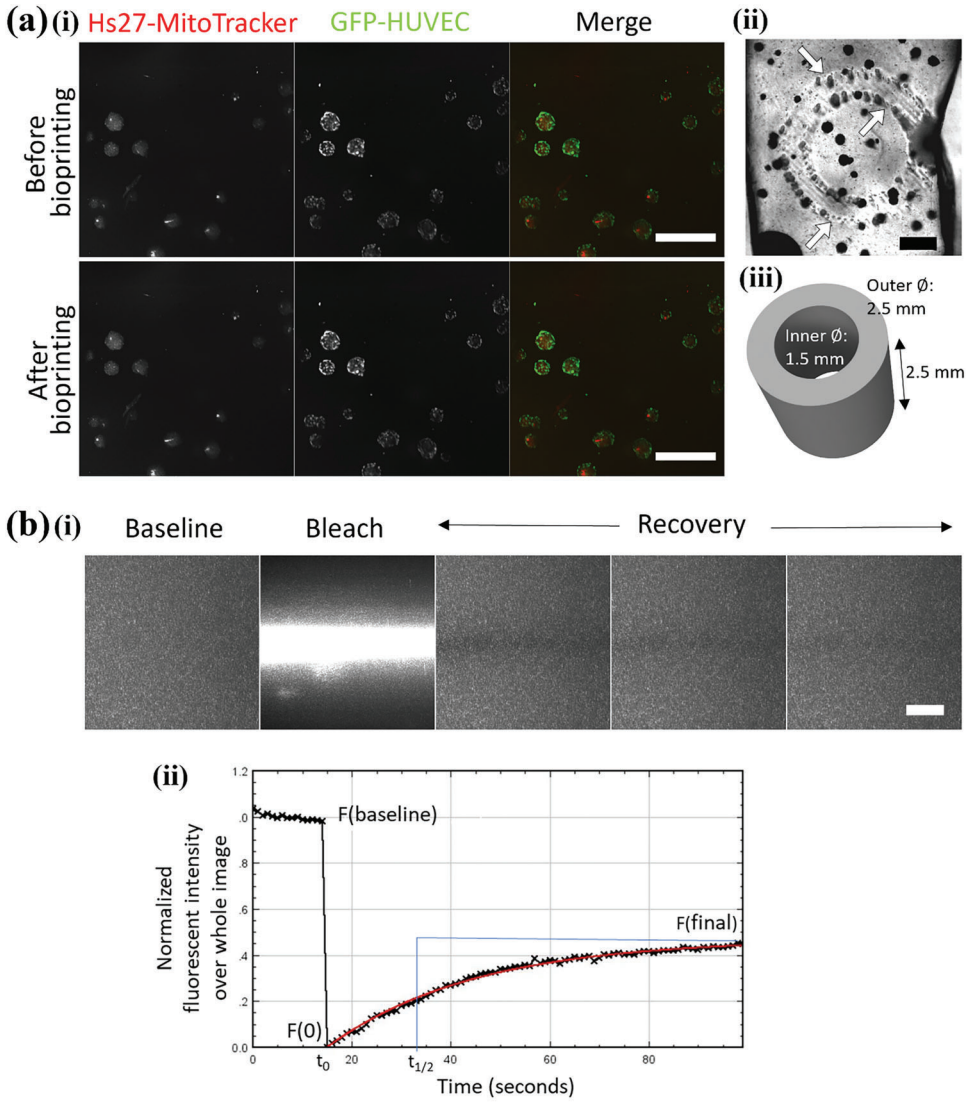

Figure 3. Streamlined imaging of key elements in the bioprinting process for advanced quality control. a) Imaging of bioprinted spheroids using an integrated light sheet fluorescence microscope in the bioprinting setup. Fibroblasts and GFP-HUVECs were co-cultured as spheroids. (i) Hs27 cells stained with MitoTrackerRed and GFP-HUVEC cells were bioprinted. Signal intensity from Hs27-MitoTracker (red) and GFP-HUVEC (green) spheroids remained consistent before and after bioprinting, and spatial positioning of the spheroids remained unchanged. Voxel size: 0.69 × 0.69 × 10 µm. Objective lenses: Zeiss A-Plan 2.5x/0.06 (excitation). Scale bar: 200 µm. (ii) Spatial arrangement of cells or spheroids can be assessed by brightfield imaging post-crosslinking. Boundaries of printed objects are indicated. Scale bar: 1000 µm. (iii) CAD rendering of the object selected for 3D bioprinting of cells (hollow cylinder). Printing intensity: 4.81 mW. b) FRAP analysis within the bioprinter setup to evaluate hydrogel crosslinking. (i) Illustration of selected z-stack slices acquired during a FRAP experiment on a crosslinked hydrogel. Baseline imaging captures initial fluorescence levels, followed by bleaching (100% laser intensity for 10 seconds) and subsequent imaging of fluorescence recovery through the bleached region (7.18 mW, 100 images per second). The bleached zone gradually repopulates with neighboring FITC-dextran molecules, eventually reaching a plateau. (ii) The fluorescent intensity of the bleached zone is normalized to a non-bleached zone and plotted against time. The half recovery time ($t_{1/2}$) is calculated using the curve-fitting parameters. Note here that the photobleaching was not taken into consideration in the analysis. (iii) Rendering of the CAD file used for the FRAP experiment: 3×3×3 mm cube. Printing intensity: 7.18 mW.

to reach this plateau (which might not correspond to the original baseline intensity) was calculated and halved to yield the half recovery time, a conventional value used to represent the diffusion speed of the molecules. A higher half recovery time would signify a slower diffusion of molecules, indicating larger pore sizes in the crosslinked hydrogel, hence a looser network with higher flow rates of nutrients and metabolites. By using established equations, such as those from Kang et al.,[35] the pore size within the hydrogel could be extrapolated from the data, allowing further quantification. Using this method, the user can therefore determine the necessary intensity to crosslink the hydrogel as desired.

All these quality control steps could be seamlessly integrated into the bioprinting process. Both imaging and bioprinting were taking place in the same sample holder and position, eliminating the need for extra steps like transferring the object onto a

well plate. This setup also holds potential for future projects that involve prolonged time-lapse imaging of cells over an extended period by using time lapse imaging.

2.4. Light Sheet Bioprinting Enables the Production of Full-Thickness Skin Tissues

Bioprinting can have detrimental effects on cell viability due to various factors like passaging, exposure to synthetic polymer solutions, and processing methods. In conventional extrusion-based bioprinting, cells may experience viability loss due to shear forces during dispensing through a nozzle, impact velocity, and droplet volume.[36–38] Similar challenges are encountered in light-based bioprinting. For instance, the wavelength used for photocrosslinking plays a role, favoring visible light over ultraviolet light to prevent cell damage.[37,39,40] Additionally, the presence of free radicals in non-crosslinked hydrogels can negatively impact cell viability. The chemical reactions involved in photocrosslinking produce radicals that, in contact with cells, can cause oxidative damage.[41–43]

Cell viability is therefore an indicator of the status of the cells after the bioprinting that measured by quantifying the number of dead cells over the total amount of cells. Using LUMINATE, human fibroblasts (Hs27 cells) were encapsulated in the Cellendes hydrogel 2 and bioprinted as a hollow cylinder to promote optimal medium diffusion. A live-dead assay conducted immediately after bioprinting (day 0) and following seven days of culture in a well-plate revealed high viability: 90% ± 8.98% (standard deviation or SD) directly after bioprinting and 83% ± 4.34% after seven days in culture (**Figure 4b i**). There was no significant difference noted between those results (Welch t-test, $p = 0.35$, $n = 3$ to 5). This outcome demonstrates that the bioprinting process and subsequent culture did not significantly affect cell viability.

In order to increase in complexity and produce more intricate and sophisticated tissues, a full-thickness construct containing Hs27 human fibroblasts and HaCaT human keratinocytes was developed. Hs27 cells were encapsulated in Cellendes hydrogel 2 and bioprinted as hollow cylinders. After three days, HaCaT cells were seeded on the construct's surface, cultured immersed for an additional seven days, before commencing the air-liquid interface (ALI) culture. Cell viability was assessed 41 days post-bioprinting and measured at 74% ± 13.25% (SD). Although a viability decrease was observed, this could potentially be counteracted by introducing more complexity to the 3D bioprinted system, such as vascularization. Certainly, the incorporation of a functional perfused vascular network, including smaller vessels, would significantly enhance nutrient supply to the cells within the bioprinted construct, particularly over extended periods. Nevertheless, despite variability between biological replicates, no significant differences were noted between day zero and day 41 (Welsh t-test, $p = 0.40$, $n = 3$ to 5).

The effect of adding the static light sheet, as previously described, was further examined. Using LUMINATE, Hs27 fibroblasts were bioprinted in hollow cylinders (laser intensity: 4.81 mW) using either a single beam or in combination with the static light sheet. Following a seven-day immersion culture, the viabilities of fibroblasts in constructs bioprinted with or without the static light sheet were comparable, measuring at 83% ± 4.34% and 78% ± 0.03% (SD), respectively (Figure 4b ii). Statistical analysis revealed no significant difference between cultures bioprinted with the single beam and the static light sheet (Welch t-test, $p = 0.22$, $n = 3$).

Upon close examination of the edge of the long-term co-culture construct (indicated by an asterisk in Figure 4a and magnified in Figure 4c), a densely packed layer of cells, likely keratinocytes, was observed. This layer exhibited a compact and moderately stratified appearance, resembling an immature epithelial layer that is commonly observed in vivo.[44] To confirm the identity of the cell types and validate the physiological significance of the bioprinted skin constructs produced using LUMINATE, an immunofluorescent staining procedure was conducted, targeting significant dermal and epidermal markers.

Employing the same hollow cylinder design (laser intensity: 12 mW), fibroblasts were encapsulated and subsequently co-cultured with keratinocytes under air-liquid interface (ALI) conditions. To explore the physiological relevance of the resulting model, immunofluorescence staining was performed on the cells and confocal microscopy was employed for imaging. In the context of our model, keratinocytes represented the epidermis, a barrier separating the external and internal environments of the body. As part of this barrier function, the keratinocytes must form a tightly interconnected layer with adhesion and tight junction proteins. Key markers for this epidermal functionality include E-cadherin, which regulates tight junctions,[45,46] and keratin 14, a constituent of intermediate filaments that reinforces the epidermal barrier and contributes to stratification.[47] They both play a part in the differentiation program of the keratinocytes into stratified layers.[48,49] Immunofluorescence staining revealed the presence of these epithelial markers (keratin 14 and E-cadherin) in the upper cell layer of the construct. This layer was located on the side exposed to air in the ALI culture, closely resembling the organization of the first stratum of the epidermis (**Figure 5a,b**).

In the dermal layer, fibroblasts represent the primary cell type, contributing to extracellular matrix (ECM) production and interactions with epidermal cells, especially during hair follicle initiation.[50–53] Vimentin, a cytoskeletal protein characteristic of fibroblasts,[54,55] was uniformly expressed within the 3D bioprinted Hs27 after 41 days in culture (Figure 5c; Video S4, Supporting Information). The significance of collagen I within the skin's ECM cannot be understated, as it serves as a fundamental component of the interstitial matrix.[56,57] Both collagen I and vimentin were consistently detected throughout the thickness of the dermis, as seen on Figure 5b,c (and Video S4, Supporting Information), reflecting their importance in maintaining the integrity and structural properties of the skin. Finally, collagen IV plays an important role as the main component of the basement membrane, the separation and support sheet-like structure between epidermis and dermis in the skin.[58,59] Its presence was observed as a distinct layer situated between the keratinocytes (upper layer) and the fibroblasts (beneath). This arrangement closely mirrors the architecture of the natural skin's basement membrane, thereby underscoring the physiological accuracy of the bioprinted model.

In the absence of keratinocytes, when fibroblasts were cultured alone, sporadic expression of vimentin and collagen IV was

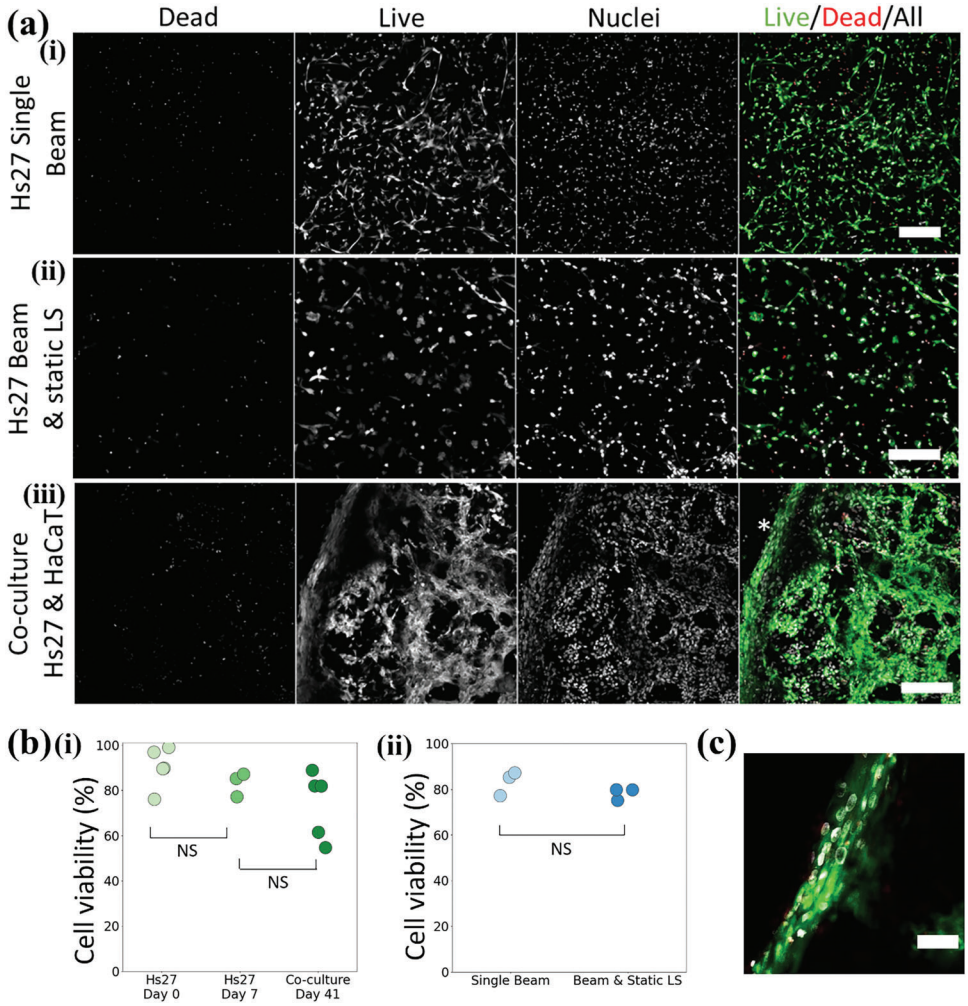

Figure 4. Assessment of cell viability in cells bioprinted using the LUMINATE device. a) Live-dead assay was conducted to assess cell viability in cell constructs bioprinted using the LUMINATE device. Different experimental setups were examined: (i) Hs27 cells encapsulated within hydrogel matrix using the light beam alone, (ii) Hs27 cells encapsulated within hydrogel matrix using a combination of the light beam and the static light sheet, and (iii) Co-culture of Hs27 fibroblasts and HaCaT keratinocytes at the air-liquid interface (ALI) conditions, stained after 41 days. Dead cells were labeled with propidium iodide (PI), viable cells with FDA (fluorescent diacetate), and the total cell population with Hoechst 33 342 (nuclei). Live cells were uniformly distributed throughout the matrix. Notably, the co-culture image exhibited tight cellular structures resembling epidermal layering, marked with an asterisk. b) Quantitative analysis of cell viability was performed by segmenting and analyzing images of FDA/PI/Hoechst-stained cells. This analysis enabled quantification of cell viability for different cell cultures encapsulated using LUMINATE. (i) Cell viability was assessed directly after bioprinting, after 7 days, and after 41 days. No significant differences were observed between day 0 and the different time points (Welch t-test, $p = 0.35$ and $p = 0.40$, day 0 – day 7 and day 0 – day 41, respectively). (ii) The cell viability between employing the patterning beam alone or in combination with the light sheet was quantified. No significant difference was observed between cultures bioprinted with the single beam alone and with a combination of patterning beam and static light sheet (Welch t-test, $p = 0.22$). c) Close-up view of the outer layer of the bioprinted construct highlights a densely packed layer of mostly live cells with a few dead cells detaching toward the outside. This image was extracted from slice 19 from 57 of the z-stack and therefore shows a single layer of cells. Light intensity by bioprinting: 4.81 – 8.23 mW. Microscope: Zeiss AxioObserver LSM780. Objective: Plan ApoChromat 20×/0.8 M27. Voxel size "Hs27 Single Beam": 0.52 × 0.52 × 6 µm. Voxel size "Hs27 Beam & static LS" and "Co-culture Hs27 & HaCaT": 0.83 × 0.83 × 6 µm. Scale bar: 100 µm.

observed, highlighting the crucial role that keratinocytes play in mediating these interactions within the co-culture system (Figure S12a,b, Supporting Information). The design incorporated 3D-bioprinted holes (500 µm in diameter) on the construct's surface, mimicking skin rete ridges. In the native skin, the dermal-epidermal junction exhibits a distinctive corrugated structure known as rete ridges. These rete ridges play a pivotal role in maintaining the functionality of keratinocyte stem cell niches and should be replicated in engineered skin tissues.[60] Remarkably, even after 41 days in culture, these ridges maintained their structural integrity and size, demonstrating the model's capacity to preserve architectural features over time (Figure S12c, Supporting Information and Figure 5c).

In summary, the immunofluorescence imaging, marker expression patterns, and architectural preservation observed within the bioprinted constructs collectively substantiated the robustness and physiological relevance of the developed skin model.

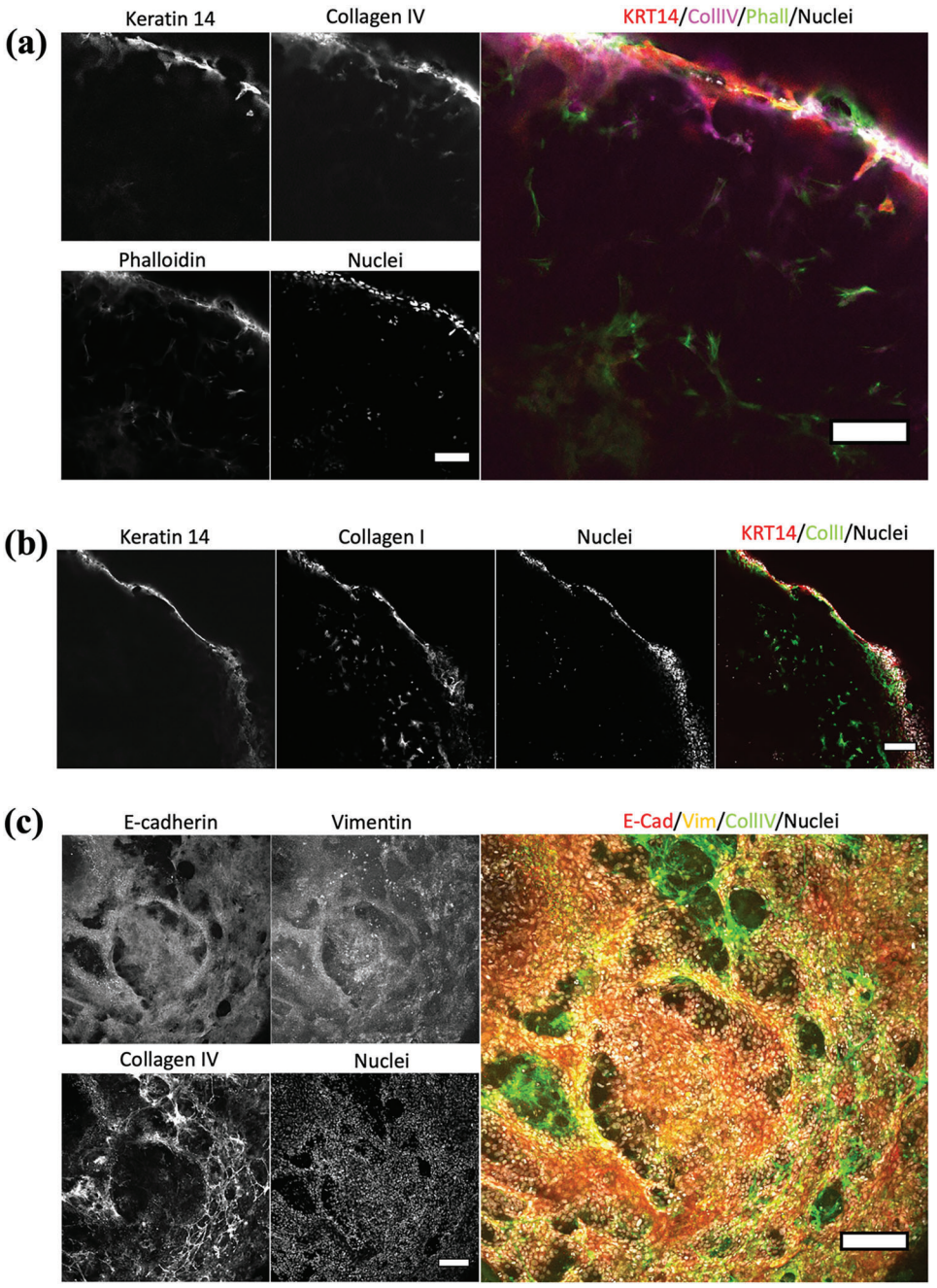

Figure 5. Characterization of the maturation levels of the full-thickness, long-term cultured 3D bioprinted constructs consisting of Hs27 fibroblasts and HaCaT keratinocytes. The immunofluorescent staining reveals distinct markers for various components of the tissue model. a) Cross-section of the ALI-cultured keratinocytes and encapsulated fibroblasts stained against cytokeratin 14 (KRT14, in red) showing the epidermis, collagen IV (CollIV, in magenta) presenting the basement membrane, phalloidin (Phall, in green) identifying the actin cytoskeleton and Hoechst (nuclei, in gray). Single slice. Voxel size: 0.83 × 0.83 × 6 µm. Scale bar: 100 µm. b) Cross-section of the co-culture of 3D bioprinted fibroblasts and keratinocytes stained against cytokeratin 14 (KRT14, in red) indicating the epidermis, collagen I (CollI, in green) depicting the dermis, and Hoechst (nuclei, in gray). Single slice. Voxel size: 1.38 × 1.38 × 5 µm. Scale bar: 200 µm. c) Imaged from above, full-thickness model with bioprinted fibroblasts and seeded keratinocytes, stained against E-cadherin (E-cad, in red) representing the epidermis, vimentin (Vim, in yellow) indicating the basement membrane, collagen IV (CollIV in green) showing the fibroblasts, and Hoechst (nuclei, in gray). Z-projection. Voxel size: 1.38 × 1.38 × 5 µm. Scale bar: 200 µm. Microscope: Zeiss AxioObserver LSM780. Objective: Plan ApoChromat 20×/0.8 M27.

3. Conclusions

The pursuit of faster and high-resolution 3D bioprinting methods has long been a central objective in the field. However, it is crucial to strike a balance between these aspects, especially ensuring that speed does not compromise resolution or the printing of intricate design geometry. Moreover, the pursuing of faster and higher-resolution devices must also align with their practical applications. Is achieving sub-micrometer resolution always essential?

In the field of tissue engineering, the inclusion of streamlined and user-friendly monitoring techniques, such as microscopy imaging that can be applied before, during, and immediately after the bioprinting process, offer significant advantages for an unbiased analysis of the construct. In this context, we introduced a groundbreaking bioprinting device dubbed LUMINATE. By leveraging the principles of light sheet microscopy, LUMINATE fabricates at high speed complex structures with similar (negative feature size) or better (positive feature size) resolution compared to volumetric bioprinting, while also integrating in situ light sheet fluorescence imaging of the construct. Light sheet imaging allows to straightforwardly assess live and in 3D both the cells and the hydrogel state immediately before and immediately after the bioprinting. Moreover, we also integrated a real-time bright-field monitoring of the laser patterning and of the construct throughout the bioprinting procedure. Our experiments using cells encapsulated in a photocrosslinkable hydrogel demonstrated robust post-bioprinting cell viability, even after extended periods of culture. Furthermore, the expression of tissue-specific markers and relevant 3D organization of the tissue were observed, underscoring the potential of the technique for generating tissue-like structures.

The versatility of the device lies also in its compatibility with alternative illumination systems. For example, volumetric illumination could be combined with the light sheet plane selectivity. To this aim, the patterning with galvanometric mirrors could be replaced by illumination with a digital micromirror device (DMD). Also, xolography-like 3D printing, i.e., using different wavelengths for light sheet and patterning beam could be easily implemented. The prospect of using the xolography approach in bioprinting is intriguing due to its high speed and high-resolution. However, its applicability to bioprinting remains open, as the more complex dual-color photoinitiator chemistry and the illumination in the ultraviolet (UV) region of the spectrum (375 nm) pose potential challenges for the compatibility of this method to operate with living cells. Overall, while volumetric bioprinting and xolography alone share some properties with LUMINATE, they lack its level of flexibility.

Two-photon bioprinting can reach sub-micrometer resolution. However, objective lenses with high numerical aperture (>0.8) are required to achieve 2-photon excitation, thus limiting the working distance of the lens and consequently the achievable size of the construct. In contrast LUMINATE can print large constructs with a spatial resolution of 9 µm, roughly the size of a single cell. Thus, the method combines high speed and large bioprinting volume without sacrificing resolution. A further key advantage of light sheet bioprinting is the low energy density (mJ cm^{-2}) required for the photo-crosslinking, which is between 20 and 50 times smaller compared to volumetric printing, due to the selective plane light sheet illumination. This offers a promising avenue for mitigating potential cell and tissue damage resulting from excessive light exposure. Thus, the combination of light sheet bioprinting and light sheet/brightfield imaging realized in LUMINATE holds promise for advancing the bioprinting and tissue engineering fields.

Despite these capabilities, some areas require further refinement. One significant challenge is reducing light scattering in the cell-laden bioink, in order to enhance both resolution and precision by improving the penetration depth of the light sheet at high cell density. Strategies like incorporating contrast agents to homogenize the refractive indices between cells and hydrogel[61] or utilizing correction masks[62] could be explored to minimize this issue. While the current limitation of printing one sample at a time hinders the generation of high-throughput drug discovery models, an inverted light sheet bioprinter setup inspired to existing inverted light sheet fluorescence microscopes could potentially adapt the technique to accommodate well-plate formats.

The current approach of "slicing" the CAD model for bioprinting remains prevalent in extrusion and stereolithography methods. This process generates a stack of 2D images projected onto the xy-axis or, in the case of volumetric bioprinting, along the rotation axis (radon transform of the CAD file). Although this work is centered on light sheet-based bioprinting, the LUMINATE system can easily switch between different illumination modalities: light sheet + scanning beam, single scanning beam alone, and even dual perpendicular scanning beams, by substituting the static light sheet with a dynamically scanned light sheet. These multiple modalities could be used to selectively change resolution and/or stiffness in different regions of the same bioprinted construct. However, the currently used slicing software does not allow to take advantage of mixed illumination modalities.

Addressing this gap would necessitate the development of slicing software capable of analyzing the structure to be printed and determining the optimal crosslinking method along with the required laser intensity. The ability to create gradients of stiffness across multiple planes, including the xy-axis in addition to the z-axis, would be a valuable tool for tissue engineering applications. This flexibility could enable the creation of tissue structures with precisely tuned mechanical properties. Moreover, the versatility of LUMINATE as demonstrated in this study implies broader applications beyond tissue engineering, such as hydrogel testing and drug discovery. The future of bioprinting is likely to involve the evolution of more versatile systems that integrate bioprinting, imaging, and quality control functionalities. LUMINATE serves as a promising platform for such future advancements.

4. Experimental Section

Materials: The porcine skin type A and methacrylic anhydride was purchased from Sigma Aldrich Chemie GmbH. The dialyzing membranes were obtained from Spectrumlabs. The freeze drier was an Alpha1-4LD from Christ and the spectrometer a DMX-500 high resolution NMR spectrometer from Brucker. The polyethylene glycol diacrylate (PEGDA), Lithium-Phenyl-2,4,6-trimethylbenzoylphosphinat (LAP), tartrazine and FITC-dextran were purchased from Sigma Aldrich Chemie GmbH. The phosphate buffer saline (PBS) was purchased from Gibco, ThermoFisher Scientific. All hydrogel components for the Cellendes hydrogel were provided by Cellendes GmbH as part of the BRIGHTER project. The Hs-27 human foreskin fibroblasts were purchased from the American Type Culture

Collection (ATCC, CRL-1634). The HaCaT human keratinocytes were purchased from Cell lines services (CLS, 300 493). Green fluorescent protein-expressing human umbilical vein endothelial cells (GFP-HUVEC) were purchased from Pelo Biotech (cAP-0001GFP). Media, supplements and cell culture consumables were purchased from ThermoFisher Scientific. Medium and supplements for the endothelial cells as well as the flask speed coating solution were purchased from Pelo Biotech. Normocin was purchased from Invivogen. The cell culture plate inserts (transwells) for 24 wells (PET membrane, 3.0 µm pore size) were purchased from VWR International.

Fluorescein isothiocyanate-dextran (FITC-dextran) was purchased from Sigma Aldrich Chemie GmbH. The antibodies and dyes were purchased and diluted according to Table S4 (Supporting Information). Paraformaldehyde (PFA) and triton X-100 were purchased from Millipore-Sigma, glycine, tween-20, and albumin fraction V (BSA) were purchased from Carl Roth GmbH. Goat serum was purchased from ThermoFisher Scientific.

The overall pictures of the bioprinted objects were taken using the Zeiss SteREO Discovery V8 stereomicroscope (Carl Zeiss GmbH). The cell viability and immunofluorescent staining pictures were taken using the Zeiss AxioObserver LSM780 confocal microscope (Carl Zeiss GmbH).

Bioprinter Setup: Optical parts were installed onto an optical breadboard, using the OWIS 45 and 65 rail system. The multi-wavelength iChrome CLE-CD laser engine was purchased from TOPTICA Photonics AG. It included four wavelengths (λ = 395/60; 488/20; 561/20; 640/20 nm/mW) in one engine. Another iChrome CLE laser engine with four wavelengths (λ = 405/20; 488/20; 561/20; 640/20 nm/mW) was used with a zoom beam expander (1x – 8x, S6ASS2075-067, Sill Optics GmbH & Co. KG) and a cylindrical lens (f = 120 mm) to create the static light sheet. Two DynAxis 3S galvanometer scanners (one for x- and one for y-axis) were purchased from SCANLAB GmbH with their respective controller boards. A telecentric f-theta lens (f = 40 mm), specifically manufactured for the use with near-UV light, was purchased from Sill Optics GmbH & Co. KG.

Objective lenses with 2.5x (EC Epiplan-Neofluar 2.5x/0.06, M27, WD: 15.1 mm) and 5x magnification (Plan-Neofluar 5x/0.16, M27, WD: 18.5 mm) from Carl Zeiss were used for illumination and detection, but could easily be replaced by other objectives with, e.g., higher or lower magnification and numerical aperture. A tube lens (Carl Zeiss, 1x, f = 164.5 mm) was used to create a real intermediate image before the light enters the objective lens. A PIFOC objective scanner (Physik Instrumente, P-725.4CD) together with a compatible controller (Physik Instrumente, E-709) was used for focusing the illumination objective. Three M-111.2DG1 compact linear stages (Physik Instrumente) were coupled with a M-116 360-degree precision rotation stage (Physik Instrumente) to allow a movement of the cuvette in four axes. A C-884 DC motor (Physik Instrumente) controller was used for steering the stages. Two 4k resolution cameras from The Imaging Source Europe GmbH were purchased for pattern observation and cuvette positioning (DFK33UX34) and for light sheet image detection (DMK33UX34). Another zoom beam expander (1x – 8x, S6ASS2075-067, Sill Optics GmbH & Co. KG.) was used to focus light into the pattern observation camera and another tube lens (Carl Zeiss, 1x, f = 164.5 mm) was placed in front of the light sheet image detection camera. A computer-controlled filter wheel and its corresponding controller (Sutter Instruments, Lambda 10–3) equipped with four filters were used to filter out non-fluorescent signals for the light sheet imaging. Light is directed into the light sheet imaging camera via a round protected silver mirror (Thorlabs, Ø1″). The specimen chamber was custom designed, and 3D printed on an Anycubic Photon Mono X using black resin (Anycubic). The chamber includes windows made of either cover glass (illumination) or FEP-foil (detection) and an insert for a temperature sensor and a heating foil, which can be controlled via a temperature regulator (Winkler, WRT-2000). Stainless steel stage holders and specimen holders were machined in-house and equipped with a magnetic head for seamless attachment to the stage.

A custom-built printed circuit board (PCB) based on an Arduino clone (PJRC, Teensy 4.1), was used to centrally connect and control the laser units, galvanometer scanners, stages, cameras, and filter wheel. Custom digital-to-analog converter boards were used to address analog inputs on some devices (laser units, galvanometer scanners). Custom digital-to-serial converter boards were used to address serial inputs on other devices (stage controller, PIFOC controller).

Bioprinter Handling and Software: A custom firmware, flashed onto a Teensy 4.1 microcontroller and written in C++, was used for controlling the bioprinter and microscope components. Functions in the software were separated for the use of microscopy and bioprinting features. The main function for bioprinting is the interpretation of G-code files. The file was read line by line by the software and based on the type of action in the G-code ("M" and "G" values) the software recognizes which hardware was addressed. Based on the localization data (xyz-coordinates) the software could perform the movement pattern of the hardware (galvanometer scanners, stage) and modulate the respective intensity and velocity settings based on the "S" and "F" values. Automatic camera exposure for one layer was set by using the "M219" value and dwell time between image exposure by using the "P" value together with a numerical value translating into milliseconds.

3D models were Designed in the Computer-Aided Design Software Fusion 360 (Autodesk).

G-code files were generated by using slicer software, in this case Slic3r (https://slic3r.org/, version 1.3.0), an open-source programe was used. A self-written Python script was developed to allow for automizing the customization ("S" and "F" values) of G-code files, which cannot be done in the slicer software. An additional feature of the script is the calculation of the total pattern track length, resulting in the total print time when divided by the scanning speed.

The sample holders used were adapted from Hötte et al. 2019.[29] The vacuum-formed ultra-thin fluorocarbon (FEP) foils cuvettes were adapted into 3 or 10 mm (length and width), so larger objects could be bioprinted. The molds for thermoforming were designed on Fusion 360 (Autodesk) and printed on 3D printers of the Anycubic Photon series (Anycubic). Laser power for the single beam (Table S1, Supporting Information) and the static light sheet (Table S2, Supporting Information) were measured at the focal points and subsequent calculations for each 3D (bio-)printed construct are listed in Table S3 (Supporting Information).

Preparation of Photocrosslinkable Hydrogels: The GelMA/PEGDA hydrogel was composed of 10% w/v gelatin methacrylate (GelMA ≈80% bloom) and 10% w/v polyethylene glycol diacrylate (PEGDA average Mn 4000) mixed with 0.2% w/v LAP and 0.025% w/v tartrazine (Table S6, Supporting Information). The gelatin methacrylate was prepared following a protocol adapted from Loessner et al. 2016.[63-65] Briefly, gelatin from porcine skin type A was dissolved in PBS at 50 °C under stirring conditions for 2 h to obtain a 10% (w/v) gelatin solution. Methacrylic anhydride (MA, 5% v/v) was added at a rate of 0.5 mL min^{-1} and the mixture was left under stirring conditions for one hour. Then, after centrifugating the solution (1200 rcf for 3 min), the reaction was stopped by adding Milli-Q water to the supernatant. The resulting mixture was dialyzed using 6–8 kDa of molecular weight cut-off (MWCO) membranes (Spectra/por) against Milli-Q water at 40 °C, replaced every four hours for three days. The pH of the dialyzed products was subsequently adjusted to 7.4. The samples were kept overnight at -80 °C and lyophilized for 4 and 5 days using a freeze drier. The degree of methacrylation was inspected using nuclear magnetic resonance (NMR) spectrometry.[66] GelMA and PEGDA with LAP were separately mixed with PBS at 65 °C for two hours then were combined, tartrazine was added and the mix was left at 37 °C for an additional hour.

The Cellendes hydrogel was composed of two precursors: a main polymer (dextran (Dex)) carrying norbornene thiol-reactive group (N-Dex), and a thiol-containing crosslinker (with a backbone of polyethylene glycol (PEG-Link). The precursors were additionally functionalized to provide a cell-friendly environment when encapsulating cells. A cell-adhesion motif (arginyl-glycyl-aspartic acid or RGD) had been added by the supplier to the main precursor (RGD-N-Dex) while a cell-degradable, matrix metalloproteinase sensitive peptide (CD) had been added by the supplier to the hyaluronic acid crosslinker (CD-HyLink). The final concentration of norbornene and thiol was adjusted to achieve different degrees of crosslinking and thus various hydrogel stiffnesses. The details of the concentrations are listed in Tables S5 and S7 (Supporting Information). The main polymer and the crosslinker were mixed with a HEPES-phosphate buffer

without phenol red (pH 7,2), water and LAP before adding the cell suspension (where applicable). In addition, the pre-gel solution contained 0.1% low melting point (LMP) agarose. For gelation of the LMP agarose, the pre-gel solution was kept on ice for at least five minutes prior to bioprinting.

Fluorescence Recovery after Photobleaching (FRAP): The RGD-N-Dex and CD-HyLink bioink was used (Cellendes hydrogel 2). The water component was replaced by FITC-dextran diluted in water (20 kDa, 1 mg mL). The hydrogel was placed in the sample holder and the bioprinting device was then used to crosslink a cuboid (3×3×3 mm^3). The microscope part of the device (as previously described) was subsequently used to image the molecular diffusion of the FITC-dextran with a 488 nm beam. First, a baseline was imaged with a light sheet (10 images taken every second at 7.18 mW). Then, the light sheet height was lowered to zero and the intensity increased to 100% (23.27 mW) so that a single beam could be used to bleach an area of the field of view (10 s). Lastly, the post-bleach recovery was imaged using the light sheet scanning for 100 repetitions at 7.18 mW, every second.

The images were analyzed using Fiji by ImageJ (version 1.53c, U. S. National Institutes of Health). A Jython script developed by Johannes Schindelin[67] was used to extract the mobile fraction and half recovery time ($t_{1/2}$), measured as follows:

$$\text{Mobile fraction} = (F(\text{final}) - F(0)) / (F(\text{baseline}) - F(0))$$
$$t_{1/2} = F(\text{final}) - F(0) \quad (1)$$

With F(final) the final recovery intensity, F(0) the intensity at t = 0 right after bleaching and F(baseline) the baseline intensity.

Cell Culture and Encapsulation in the Photocrosslinkable Hydrogel: The cells were handled in sterile conditions and cultured in an incubator at 37 °C and 5% CO2. The Hs27 cells and HaCaT cells in DMEM supplemented with 4.5 g L^{-1} glucose and 2 mM glutamine. Both media were also supplemented with 10% fetal bovine serum (FBS) and 1% penicillin/streptomycin (PenStrep). The GFP-HUVEC cells were cultured with the provided medium, supplements and antibiotics from Pelo Biotech. The cells were cultured in 25 or 75 cm^2 flasks, coated with the speed coating solution (Pelo Biotech), the medium was changed every two to three days and the cells passaged every week.

The hydrogel used to encapsulate cells was Cellendes hydrogel 2 (Table S7, Supporting Information). To encapsulate the cells in the hydrogel before 3D bioprinting, the cells were detached from the flask using Accutase and collected by centrifugation in a pellet (300 rcf, 5 min). The supernatant was discarded, and the cells were resuspended in the previously prepared hydrogel (see previous sections) with a density of 2 million cells/ml. The agarose was added (to keep the cells in suspension) and the cell/hydrogel mixture was kept on ice for at least 5 min or until photocrosslinking. The cell/hydrogel mixture was pipetted into the cuvette (the 3 mm cuvette contained 3 µL, the 10 mm cuvette contained 1000 µL) which was sealed and brought to the bioprinter. After bioprinting, the 3 mm cuvette was opened using a scalpel and the construct was extracted using a metal spatula (the 10 mm cuvette had a big enough opening to extract objects without cutting it open). The bioprinted objects were washed in PBS supplemented with 1:500 Normocin to prevent potential contamination linked to handling and are subsequently cultured in a well plate.

In the case of a Hs27 and HaCaT co-culture, the fibroblasts-rich construct was 3D-bioprinted as described above, introduced to the upper compartment of a transwell and subsequently incubated in the medium for 3 days. The HaCaT human keratinocytes were then passaged and the medium/cell mixture (1 million cells/mL, 400 000 cells/well) was pipetted on top of the bioprinted constructs. The immersed culture was maintained for an additional 7 days. Thereafter, the medium contained on the upper part of the transwell was removed while the medium in the lower part of the transwell remained, as is required in an air-liquid (ALI) culture. These conditions were maintained for 41 days with medium changes of the lower compartment every other day.

The Hs27 and GFP-HUVEC co-culture was performed by co-culturing the cells as spheroids in a Sphericalplate 5D well-plate (Kugelmeier Ltd). Each well contained 750 microwells. The spheroids were composed of 1500 cells and were a combination of 2:1 Hs27 to GFP-HUVEC. The Hs27 cells were incubated in MitoTracker Red CMXRos (ThermoFisher) for 15 min in a serum-free medium prior to the spheroid formation, as indicated in Table S4 (Supporting Information). The culture medium used for the co-culture was a mix of 50% Hs27 medium and 50% GFP-HUVEC. After 48 h of culture in the Spherical plate, the spheroids were collected and encapsulated in the Cellendes hydrogel for imaging and bioprinting.

The specifications for bioprinting are included in Table S3 (Supporting Information). The energy dose required to bioprint the object (a hollow cylinder in the case of cell encapsulation) might vary on the volume of medium left with the centrifugated pellet. Although one tried to minimize the volume as much as possible, when the volume was high, the hydrogel was slightly diluted and the energy required for crosslinking needed to be higher. The energy ranged from 5.02 to 10.30 mJ cm^{-2}.

Cell Viability and Immunofluorescence Staining: The viability of cells after bioprinting was assessed using a propidium iodide (PI) and fluorescein diacetate (FDA) staining. The bioprinted constructs were extracted from the cuvette, washed with warmed PBS, then incubated at 37 °C for 15 min in medium without supplements and phenol red, that contained 1:100 PI, 1:500 FDA and 1:500 Hoechst (nucleus stain). After incubation, the constructs were once more washed in PBS and imaged in medium.

The immunofluorescence staining followed a previous protocol[64]. All the steps were performed at room temperature except otherwise indicated. Briefly, the bioprinted constructs were fixed in 4% PFA in PBS for 30 min, then washed thrice in PBS. Permeabilization followed using Triton X-100 (0.3% v/v) in PBS for 40 min before washing thrice in 0.1 M glycine in PBS and thrice in 0.1% Triton X-100 in PBS (PBS-T). The samples were subsequently blocked for 1 h in a freshly prepared blocking solution (10% goat serum in BSA (0.1%), Triton X-100 (0.2%), Tween-20 (0.05%) in PBS). The primary antibodies (Table S4, Supporting Information) were diluted in blocking solution and incubated at 37 °C overnight. On the next day, the samples were washed in PBST-T thrice before incubating in the secondary antibody solution (also diluted in blocking solution) for 2 h at 37 °C. A final wash with PBS-T (three times) was performed before imaging in 2% penicillin/streptomycin in PBS. The list of antibodies and dyes is provided in Table S4 (Supporting Information).

Image Processing and Statistical Analysis: Image processing was conducted in Fiji by ImageJ[68] (version 1.53c, U. S. National Institutes of Health). The images were cropped and brightness and contrast were adjusted. The images captured within the bioprinter were additionally deconvoluted using the PSF generator[69,70] and DeconvolutionLab2[71] plugins. The data produced by the live-dead assays and the immunofluorescent staining was processed using ImageJ. The images presented in this work are z-projections of the recorded z-stacks , unless otherwise specified. To quantify the live-dead assay data, the cells stained in the dead channel (PI staining) and the nuclei channel (Hoechst 33 342) were separately counted. A Gaussian blur filter was applied to images (radius 2.0), then an intensity threshold was applied so that a binary image of the cells was created. When necessary, a watershed algorithm was additionally used to separate adjacent cells. Finally, the 3D object counter plugin[72] was applied to count the number of cells segmented.

The statistical analysis was conducted on Python 3.9 (Python software foundation). The samples' normality was tested with a Shapiro-Wilk test ($p>0.01$). Subsequently, statistical comparison between two groups was tested with Welch t-test ($p<0.01$). Exact p-value resulting from the tests are included in the text. Plots were generated on Python using the Pandas[73] Seaborn[74] and Matplot[75] libraries. Graphical figures were created using Biorender.com.

Supporting Information

Supporting Information is available from the Wiley Online Library or from the author.

Acknowledgements

The authors would like to thank all the collaborators of the BRIGHTER consortium: Gustaf Mårtensson, Helmut Wurst, Brigitte Angres, and Ruby Shalom-Feuerstein. The authors thank Angela Cirulli for her assistance in testing the hydrogel preparation and for the hydrogel crosslinking and the cell culture protocols. The authors also thank Sven Plath and the Mechanical Workshop of the Biological Faculty at Goethe Universität Frankfurt for helping with the assembly of the first prototype and for their continuous support throughout this project. The authors would like to thank Janus Mosbacher for developing the custom Python G-code manipulation script. The authors thank the EU Horizon2020 project BRIGHTER (Grant #828931), the EU Horizon-EIC-2021 project B-BRIGHTER (Grant #101057894), and the German Space Agency at DLR (Grant #50W2019 and #50WB2316)for funding.

Open access funding enabled and organized by Projekt DEAL.

Conflict of Interest

FP, EHKS, EM, and NT declare that a patent has been filed related to the topics in this work (WO2022034042A1; DEVICE AND METHOD FOR STEREOLITHOGRAPHIC 3D PRINTING). The authors declare that they have no other conflict of interest.

Author Contributions

L.H and L.B. contributed equally to this work. F.P. and L.H. designed the bioprinter. L.H. assembled and tested the optical components, designed the patterning function and tested the software and electronics together with LRP. Controller software was written by L.R.P. CADs were designed by L.B. and L.H. and imaged by L.H. LB and LH designed the experiments relating to resolution and LH conducted them. Hydrogel testing experiments (FRAP) were designed and conducted by L.B. N.T. produced the gelatin methacrylate. E.M. and N.T. provided the cells, designed cell encapsulating protocols, and conducted preliminary tests on the hydrogels and their compatibility with cells. L.B. conducted the experiments involving culturing, bioprinting, imaging, viability, and immunostaining of cells. F.P., L.B., and L.H. wrote the manuscript. Support to research was provided by E.H.K.S. The research was conceived and supervised by F.P. All the authors read and revised the manuscript.

Data Availability Statement

The data that support the findings of this study are available in Supporting Information of this article.

Keywords

biofabrication, full-thickness skin model, light sheet bioprinter, light sheet fluorescence microscopy, tissue engineering

Received: June 28, 2023
Revised: October 4, 2023
Published online: December 7, 2023

[1] B. Fine, G. Vunjak-Novakovic, *ACS Biomater. Sci. Eng.* **2017**, *3*, 1884.
[2] P. Mcgonigle, B. Ruggeri, *Biochem. Pharmacol.* **2014**, *87*, 162.
[3] T. Hartung, *Parkinsonism Relat. Disord.* **2008**, *14*, S81.
[4] "S.5002 –117th Congress (2021-2022): FDA Modernization Act 2.0 | Congress.gov | Library of Congress," can be found under https://www.congress.gov/bill/117th-congress/senate-bill/5002, n.d.
[5] Organ Donation and Transplantation, https://data.hrsa.gov/topics/health-systems/organ-donation, n.d.
[6] R. P. H. Meier, A. Longchamp, M. Mohiuddin, O. Manuel, G. Vrakas, D. G. Maluf, L. H. Buhler, Y. D. Muller, M. Pascual, *Xenotransplantation* **2021**, *28*, 12681.
[7] D. F. V. Rey, J. P. St-Pierre, *Handb. Tissue Eng. Scaffolds* **2019**, *1*, 109.
[8] V. Mironov, T. Boland, T. Trusk, G. Forgacs, R. R. Markwald, *Trends Biotechnol.* **2003**, *21*, 157.
[9] M. Dey, I. T. Ozbolat, *Sci. Rep.* **2020**, *10*, 14023.
[10] WK74668 New Guide for Bioinks and Biomaterial Inks Used in Bioprinting Tissue-Engineered Medical Products, https://www.astm.org/workitem-wk74668, n.d.
[11] T. Jiang, J. G. Munguia-Lopez, S. Flores-Torres, J. Kort-Mascort, J. M. Kinsella, *Appl. Phys. Rev.* **2019**, *6*, 11310.
[12] X. Li, B. Liu, B. Pei, J. Chen, D. Zhou, J. Peng, X. Zhang, W. Jia, T. Xu, *Chem. Rev.* **2020**, *120*, 10793.
[13] S. Santoni, S. G. Gugliandolo, M. Sponchioni, D. Moscatelli, B. M. Colosimo, *Bio-Des. Manuf.* **2021**, *5*, 14.
[14] D. Yoo, D. Choi, D. S. Kim, M. Okano, S. Uemura, Y. Tabe, W. L. Ng, J. M. Lee, M. Zhou, Y.-W. Chen, K.-X. A. Lee, W. Y. Yeong, Y.-F. Shen, *Biofabrication* **2020**, *12*, 022001.
[15] L. L. Nam, N. Hibino, *3D Bioprinting: What Does the Future Hold?* **2019**.
[16] B. Zhang, R. Cristescu, D. B. Chrisey, R. J. Narayan, *IJB* **2020**, *6*, 211.
[17] P. N. Bernal, P. Delrot, D. Loterie, Y. Li, J. Malda, C. Moser, R. Levato, *Adv. Mater.* **2019**, *31*, 1904209.
[18] Z. Zheng, D. Eglin, M. Alini, G. R. Richards, L. Qin, Y. Lai, *Engineering* **2021**, *7*, 966.
[19] M. Regehly, Y. Garmshausen, M. Reuter, N. F. König, E. Israel, D. P. Kelly, C. Y. Chou, K. Koch, B. Asfari, S. Hecht, *Nature* **2020**, *588*, 620.
[20] M. T. Raimondi, S. M. Eaton, M. M. Nava, M. Laganà, G. Cerullo, R. Osellame, *J. Appl. Biomater.* **2012**, *10*, 55.
[21] D. Perevoznik, R. Nazir, R. Kiyan, K. Kurselis, B. Koszarna, D. T. Gryko, B. N. Chichkov, *Opt. Express* **2019**, *27*, 25119.
[22] G. Poologasundarampillai, A. Haweet, S. N. Jayash, G. Morgan, J. E. Moore, A. Candeo, *Int. J. Bioprint.* **2021**, *23*, 00144.
[23] Next-Generation Bioprinting – Poietis –4D Bioprinting | Next Generation Bioprinting, https://poietis.com/ngb/, n.d.
[24] J. Huisken, J. Swoger, F. Del Bene, J. Wittbrodt, E. H. K. Stelzer, *Science 1979* **2004**, *305*, 1007.
[25] P. J. Keller, F. Pampaloni, E. H.k Stelzer, *Curr. Opin. Cell Biol.* **2006**, *18*, 117.
[26] P. J. Keller, E. H. K. Stelzer, *Cold Spring Harb. Protoc.* **2010**, *5*, pdb.top78.
[27] P. J. Keller, A. D. Schmidt, J. Wittbrodt, E. H. K. Stelzer, *Science* **2008**, *322*, 1065.
[28] Switzerland. International Organization for Standardization, Geneva, **2009**.
[29] K. Hötte, M. Koch, L. Hof, M. Tuppi, T. Moreth, M. M. A. Verstegen, L. J. W. van der Laan, E. H. K. Stelzer, F. Pampaloni, *Sci. Rep.* **2019**, *9*, 17292.
[30] S.-M. Yu, B. Li, F. Amblard, S. Granick, Y.-K. Cho, *Biomaterials* **2021**, *265*, 120420.
[31] D. F. Swinehart, *J. Chem. Educ.* **1962**, *39*, 333.
[32] K. Bialkowska, P. Komorowski, M. Bryszewska, K. Milowska, *Int. J. Mol. Sci.* **2020**, *21*, 6225.
[33] J. Karvinen, T. O. Ihalainen, M. T. Calejo, I. Jönkkäri, M. Kellomäki, *Mater. Sci. Eng.: C* **2019**, *94*, 1056.
[34] N. R. Richbourg, N. A. Peppas, *Macromolecules* **2021**, *54*, 10477.
[35] M. Kang, C. A. Day, A. K. Kenworthy, E. DiBenedetto, *Traffic* **2012**, *13*, 1589.
[36] K. Nair, M. Gandhi, S. Khalil, K. C. Yan, M. Marcolongo, K. Barbee, W. Sun, *Biotechnol. J.* **2009**, *4*, 1168.
[37] R. Chang, J. Nam, W. Sun, *Tissue Eng. Part A* **2008**, *14*, 41.

[38] W. L. Ng, X. Huang, V. Shkolnikov, G. L. Goh, R. Suntornnond, W. Y. Yeong, *Int. J. Bioprint.* **2022**, *8*, 424.
[39] K. P. Lawrence, T. Douki, R. P. E. Sarkany, S. Acker, B. Herzog, A. R. Young, *Sci. Rep.* **2018**, *8*, 12722.
[40] D. Y. Wong, T. Ranganath, A. M. Kasko, *PLoS One* **2015**, *10*, 139307.
[41] A. Eibel, D. E. Fast, G. Gescheidt, *Polym. Chem.* **2018**, *9*, 5107.
[42] M. Del Carlo, R. F. Loeser, *Arthritis Rheum.* **2003**, *48*, 3419.
[43] B. Halliwell, J. M. C. Gutteridge, *Free Radicals in Biology and Medicine*, Oxford University Press, Oxford **2015**.
[44] M. Tsunenaga, Y. Kohno, I. Horii, S. Yasumoto, N.-h Huh, T. Tachikawa, S. Yoshiki, T. Kuroki, *Japanese Journal of Cancer Research* **1994**, *85*, 238.
[45] J. A. Tunggal, I. Helfrich, A. Schmitz, H. Schwarz, D. Günzel, M. Fromm, R. Kemler, T. Krieg, C. M. Niessen, *EMBO J.* **2005**, *24*, 1146.
[46] F. Furukawa, K. Fujii, Y. Horiguchi, N. Matsuyoshi, M. Fujita, K.-I. Toda, S. Imamura, H. Wakita, S. Shirahama, M. Takigawa, *Microsc. Res. Tech.* **1997**, *38*, 343.
[47] Y. Guo, C. J. Redmond, K. A. Leacock, M. V. Brovkina, S. Ji, V. Jaskula-Ranga, P. A. Coulombe, *Elife* **2020**, *9*, 53165.
[48] H. Alam, L. Sehgal, S. T. Kundu, S. N. Dalal, M. M. Vaidya, *Mol. Biol. Cell* **2011**, *22*, 4068.
[49] P. A. Coulombe, R. Kopan, E. Fuchs, *J. Cell Biol.* **1989**, *109*, 2295.
[50] R. Sennett, M. Rendl, *Semin. Cell Dev. Biol.* **2012**, *23*, 917.
[51] R. R. Driskell, F. M. Watt, *Trends Cell Biol.* **2015**, *25*, 92.
[52] D. Chen, A. Jarrell, C. Guo, R. Lang, R. Atit, *Development* **2012**, *139*, 1522.
[53] M. A. Kisiel, A. S. Klar, *Methods Mol. Biol.* **2019**, *1993*, 71.
[54] Tissue expression of VIM – Summary – The Human Protein Atlas, https://www.proteinatlas.org/ENSG00000026025-VIM/tissue, n.d.
[55] T. Kueper, T. Grune, S. Prahl, H. Lenz, V. Welge, T. Biernoth, Y. Vogt, G. M. Muhr, A. Gaemlich, T. Jung, G. Boemke, H. P. Elsässer, K. P. Wittern, H. Wenck, F. Stäb, T. Blatt, *J. Biol. Chem.* **2007**, *282*, 23427.
[56] K. Henriksen, M. A. Karsdal, in *Biochemistry of Collagens, Laminins and Elastin: Structure, Function and Biomarkers* (Eds.: M. A. Karsdal, D. J. Leeming, K. Henriksen, A.-C. Bay-Jensen, S. Holm Nielsen, C. L. Bager), Academic Press, London **2019**, pp. 1–12.
[57] E. H. Epstein, N. H. Munderloh, *J. Biol. Chem.* **1978**, *253*, 1336.
[58] A. Abreu-Velez, M. Howard, *N Am J Med Sci* **2012**, *4*, 1.
[59] D. Breitkreutz, I. Koxholt, K. Thiemann, R. Nischt, *Biomed Res. Int.* **2013**, *2013*, 179784.
[60] M. Aleemardani, M. Zivojin, T. Triki´c, N. H. Green, F. Claeyssens, S. Naghieh, G. Lindberg, *Bioengineering* **2021**, *8*, 148.
[61] P. N. Bernal, M. Bouwmeester, J. Madrid-Wolff, M. Falandt, S. Florczak, N. G. Rodriguez, Y. Li, G. Größbacher, R. Samsom, M. van Wolferen, L. J. W. van der Laan, P. Delrot, D. Loterie, J. Malda, C. Moser, B. Spee, R. Levato, *Adv. Mater.* **2022**, *34*, 2110054.
[62] J. Madrid-Wolff, A. Boniface, D. Loterie, P. Delrot, C. Moser, *Adv. Sci.* **2022**, *9*, 2105144.
[63] A. I. Van Den Bulcke, B. Bogdanov, N. De Rooze, E. H. Schacht, M. Cornelissen, H. Berghmans, *Biomacromolecules* **2000**, *1*, 31.
[64] D. Loessner, C. Meinert, E. Kaemmerer, L. C. Martine, K. Yue, P. A. Levett, T. J. Klein, F. P. W. Melchels, A. Khademhosseini, D. W. Hutmacher, *Nat. Protoc.* **2016**, *11*, 727.
[65] A. Vila, N. Torras, A. G. Castaño, M. García-Díaz, J. Comelles, T. Pérez-Berezo, C. Corregidor, Ó. Castaño, E. Engel, V. Fernández-Majada, E. Martínez, *Biofabrication* **2020**, *12*, 025008.
[66] X. Li, S. Chen, J. Li, X. Wang, J. Zhang, N. Kawazoe, G. Chen, *Polymers* **2016**, *8*, 269.
[67] Analyze FRAP movies with a Jython script – ImageJ, https://imagej.net/Analyze_FRAP_movies_with_a_Jython_script, n.d.
[68] J. Schindelin, I. Arganda-Carreras, E. Frise, V. Kaynig, M. Longair, T. Pietzsch, S. Preibisch, C. Rueden, S. Saalfeld, B. Schmid, J. Y. Tinevez, D. J. White, V. Hartenstein, K. Eliceiri, P. Tomancak, A. Cardona, *Nat. Methods* **2012**, *9*, 676.
[69] H. Kirshner, F. Aguet, D. Sage, M. Unser, *J. Microsc.* **2013**, *249*, 13.
[70] H. Kirshner, D. Sage, 3D PSF Models for Fluorescence Microscopy in ImageJ, n.d.
[71] D. Sage, L. Donati, F. Soulez, D. Fortun, G. Schmit, A. Seitz, R. Guiet, C. Vonesch, M. Unser, *Methods* **2017**, *115*, 28.
[72] S. Bolte, F. P. Cordelières, *J. Microsc.* **2006**, *224*, 213.
[73] W. McKinney, *Proceedings of the 9th Python in Science Conference* **2010**, *445*, 51.
[74] M. Waskom, *J. Open Source Softw.* **2021**, *6*, 3021.
[75] J. D. Hunter, *Comput. Sci. Eng.* **2007**, *9*, 90.
[76] O. Svelto, *Principles of Lasers*, Springer, New York **2010**.
[77] E. H. K. Stelzer, *Nat. Methods* **2015**, *12*, 23.